An experimental investigation on two-dimensional shape-based diffuse optical tomography

Pingqiao Ruan (阮平巧)[1], Feng Gao (高 峰)[1,2*], Fang Yang (杨 芳)[1], and Huijuan Zhao (赵会娟)[1,2]

[1] *College of Precision Instrument and Optoelectronics Engineering, Tianjin University, Tianjin 300072, China*

[2] *Tianjin Key Laboratory of Biomedical Detecting Techniques and Instruments, Tianjin 300072, China*

[*] *E-mail: gaofeng@tju.edu.cn*

Received January 26, 2010

A two-dimensional (2D) shape-based approach of image reconstruction using a boundary element method is developed for diffuse optical tomography (DOT). The experimental validation uses a four-channel time-correlated single photon counting (TCSPC) system for detection and an intensity data-type for image reconstruction. The optical and geometric parameters are simultaneously recovered using a difference imaging scheme. Results demonstrate that the proposed DOT modality is a promising methodology of *in vivo* reconstruction of the optical structures of tissues.

OCIS codes: 170.3880, 170.6960, 170.3010, 170.3660.

doi: 10.3788/COL20100808.0787.

Fluorescence molecular tomography (FMT) is a novel optical imaging modality for visualizing the biochemical events located deep inside intact living organisms with molecule-specific fluorescent agent[1]. Researchers have demonstrated that knowledge on optical properties distribution in tissues significantly affects FMT[2]. To provide optical priors for enhanced fluorescence reconstruction, a combination of FMT and diffuse optical tomography (DOT) is desirable.

DOT is a noninvasive medical imaging technology that probes internal optical properties and can provide both anatomical images and functional information of tissues. However, due to the strong scattering nature of most tissue types and relatively limited number of available noisy data, image reconstruction in conventional voxel-based DOT has been a severely ill-posed inverse problem[3]. One way of improving this situation is to take advantage of prior information on the probability distribution of expected parameters based on anatomical structures[4,5].

The use of the anatomical structures has allowed for the reasonable postulation of the unknown body as being composed of a number of sub-domains of different tissues, and the interior optical parameter values as a piecewise constant. In this case, we can parameterize the unknowns of the inverse problem directly in terms of a small number of parameters describing the shape, location, and optical properties of each region. Since unknown boundaries are typically modeled with some parametric shape functions, the image reconstruction can thus be cast as a shape-based DOT issue in order to simultaneously recover the boundary-describing parameters and optical properties of disjoint domains[6].

With the recent advancement of DOT, the shape-based image reconstruction schemes have also been proposed. The use of boundary element method (BEM) for shape-based imaging in DOT has been reported[4]. In that work, the authors recovered the shape and optical properties of an inclusion from simulated DOT data using an alteration strategy and based on the assumption that background values are known and exact. In this letter, a two-dimensional (2D) shape-based reconstruction scheme for steady-state DOT is validated by a cylindrical phantom. A difference imaging scheme is used to handle noisy measurement data, as well as to achieve more accurate parameter estimation. The optical coefficients of the background are assumed as unknown and recovered in the reconstruction.

The diffusion approximation (DA) with Robin boundary condition has been frequently used in the modeling of light propagation for biological tissues[4]. Based on the assumption on multi-domain geometries, $\Omega = \cup_{\ell=1}^{L}\Omega_\ell$, which are separated by smooth interfaces Γ_ℓ ($\ell = 2, \cdots, L$), and with the piecewise constant optical properties, the steady-state formulation of the diffusion approximation was equivalent to a set of coupled Helmholtz equations[7]:

$$\nabla^2\Phi_\ell(\mathbf{r}) - k_\ell^2\Phi_\ell(\mathbf{r}) = -\frac{q_\ell(\mathbf{r})}{\kappa_\ell},\ \mathbf{r}\in\Omega_\ell,\ \ell = 1, 2, \cdots, L \quad (1)$$

with boundary conditions

$$\Phi_{\ell-1} = \Phi_\ell, \kappa_{\ell\text{-}1}\hat{\mathbf{n}}\cdot\nabla\Phi_{\ell-1} = \kappa_\ell\hat{\mathbf{n}}\cdot\nabla\Phi_\ell \quad \text{on} \quad \Gamma_\ell,$$
$$c\Phi_1 + 2\kappa_1\frac{1+R_f}{1-R_f}\hat{\mathbf{n}}\cdot\nabla\Phi_1 = 0 \quad \text{on} \quad \partial\Omega, \quad (2)$$

where $\Phi_\ell(\mathbf{r})$ is the photon density; $q_\ell(\mathbf{r})$ denotes an interior isotropic source density in domain ℓ; the wave numbers k_ℓ associated with the Helmholtz equation in each domain has the form of $k_\ell^2 = \mu_{a\ell}c/\kappa_\ell$, c is the speed of light in the medium, $\mu_{a\ell}$, $\mu'_{s\ell}$, and $\kappa_\ell = c/[3\mu'_{s\ell}]$ are the absorption, reduced scattering, and diffusion coefficients, respectively; $\hat{\mathbf{n}}$ denotes unit normal vector outward to the boundary; and R_f is an internal reflection factor that accounts for the difference in the refractive indices between the two sides of the most outer boundary, $\partial\Omega$.

If the closed interfaces Γ_ℓ are sufficiently smooth, they can be approximated by the Fourier curve. With the shape coefficients $\gamma_\ell = \{\gamma_n^{x_\ell}, \gamma_n^{y_\ell}\}$ for the boundaries of each inner domain defined, the parametric description of the curve was represented by the weighted average de-

 © 2010 Chinese Optics Letters

rived from a set of relevant basis functions[6]:

$$\Gamma_\ell = \begin{cases} x_\ell(\theta) = \sum_{n=1}^{N_\theta} \gamma_n^{x_\ell} Y_n(\theta) \\ y_\ell(\theta) = \sum_{n=1}^{N_\theta} \gamma_n^{y_\ell} Y_n(\theta) \end{cases}, \theta \in [0, 2\pi], \quad (3)$$

where N_θ is the number of the basis functions and Y_n denotes the periodic and differentiable basis functions. We used $N_\theta = 5$ basis functions for the curve representation in the inverse computations.

The BEM approach was the natural choice for shape-based DOT since the boundaries that were discretized in the boundary integration approach were simply the unknowns of the inverse problem[7]. By applying the collocation BEM to the forward problem given in Eq. (1), we finally obtained a set of linear equations with the following matrix notation:

$$\mathbf{T}(\{\gamma_\ell, \mu_{a\ell}, \kappa_\ell\})\mathbf{\Phi} = \mathbf{Q}. \quad (4)$$

In the above equation, matrix $\mathbf{T}(\{\gamma_\ell, \mu_{a\ell}, \kappa_\ell\})$ is in a form of densely asymmetric blocks and depends nonlinearly on the boundary-description complexity of domains and their interior optical properties. The measurable flux at the most outer boundary site, $\xi_d \in \partial\Omega$ $(d = 1, 2, \cdots, \mathrm{D})$, with respect to the excitation source at $\zeta_s \in \partial\Omega$ $(s = 1, 2, \cdots, \mathrm{S})$, was calculated by solving the matrix equation and by applying Fick's law. The above mentioned process was defined as a nonlinear forward operator $\mathbf{F}(\{\gamma_\ell, \mu_{a\ell}, \kappa_\ell\})$, indicating that it maps the boundary shape parameters of γ_ℓ and the optical properties of $\{\mu_{a\ell}, \kappa_\ell\}$ to the data measured on the boundary of $\partial\Omega$.

The inverse problem considered in this letter was the simultaneous reconstruction of shape parameters and interior optical parameters from the boundary measurement, $\mathbf{y}$. This measurement was set as an optimization problem-seeking configuration for the boundary and optical parameters of the domains that minimize the distance between measured data $\mathbf{y}$ and model-predicted $\mathbf{F}(\{\gamma_\ell, \mu_{a\ell}, \kappa_\ell\})$. The inverse problem was solved within a framework of nonlinear cost-minimization. Levenberg Marquardt method was used for deriving the solution to the resultant linear system at each iteration stage. The iterative procedure is expressed as

$$\mathbf{x}_{k+1} = \mathbf{x}_k + (\mathbf{J}_k^{\mathrm{T}}\mathbf{J}_k + \lambda\mathbf{D}_k^{\mathrm{T}}\mathbf{D}_k)^{-1}\mathbf{J}_k^{\mathrm{T}}(\mathbf{y} - \mathbf{F}(\mathbf{x}_k)), \quad (5)$$

where $\mathbf{x}$ denotes the set of the unknowns to be reconstructed $\{\gamma_\ell, \mu_{a\ell}, \kappa_\ell\}$; $\mathbf{D}$ is a regularization matrix, and λ is the dumping factor; and k denotes the iteration number. The Jacobian matrix $\mathbf{J} = \partial\mathbf{F}/\partial\mathbf{x}$ was defined as a derivative of the forward mapping $\mathbf{F}(\{\gamma_\ell, \mu_{a\ell}, \kappa_\ell\})$ with respect to parameter $\mathbf{x}$, which was calculated using a finite difference method. In our implementation, a diagonal form of $\mathbf{D}^{\mathrm{T}}\mathbf{D}$ was taken. Diagonal elements were used as the norm of each column of the Jacobian matrix.

To validate the performance of the image reconstruction algorithm using experimental measurements, a four-channel time-correlated single photon counting (TCSPC) system (SPC-134, Becker & Hickl) and a cylindrical phantom with a single inclusion were used. A picosecond pulsed diode laser (PDL-828 controller with a LHD-P-830 laser head, PicoQuant) at a repetition frequency of 80 MHz and peak power of about 300–400 μW was used to emit light pulses at a duration of about 50 ps and wavelength of 830 nm into the phantom. The optode used was a bundle of two fibers with a diameter of 500 μm and a numerical aperture (NA) of 0.37; one was used for illumination and the other for detection, and hence, $\xi_i = \zeta_i$. Source delivery and signal collection were performed at 16 boundary sites using a 16×1 optical switch connected to the laser output and four 4×1 switches connected to 4 cooled photomultiplier tube (PMT) modules (PMT-100-20, Becker & Hickl) of the 4 TCSPC channels. As a result of multiple scattering, the light pulse exiting from the biological tissue in response to the excitation of the ultrashort pulsed laser, referred to as the temporal point spread function (TPSF), depicted broad distribution of photon path lengths. The TPSF was reliably measured by the TCSPC system. The detailed implementation of the system was discussed in a previous work[1].

The phantom was made of polyoxymethylene with a diameter of 55 mm and a height of 80 mm. Two phantoms were used; one was maintained as homogeneous while the other had a hole with 20-mm diameter drilled 10 mm away from the boundary (Fig. 1(a)). The hole in the phantom was then filled with 0.0069% India ink for absorption and 1.5% intralipid for scattering. The absorption coefficient (μ_a) of the India ink at 830 nm was measured using a spectrometer (HR2000, Ocean Inc.) and found to be about 0.015 mm^{-1}. The scattering coefficient (μ'_s) of the intralipid was calculated according to literature and found to be about 1.5 mm^{-1}[8,9]. The two values were adopted as estimates of μ_a and μ'_s of the inclusion. The background absorption and scattering coefficients of the homogeneous cylindrical phantom at the wavelength of 830 nm were determined as 0.0044 and 1.69 mm^{-1}, respectively. The curve-fitting algorithm best matched the normalized Laplace-transforms of the measured TPSFs compared with their model-predicted counterparts for the homogeneous phantom.

Figure 1 illustrates the sketch of the cylindrical phantom and the experimental setup. A total of 16 optodes were equally placed on the phantom in a single plane at the mid-height of the phantom. The 16 detection fibers in the optodes collected the exiting photons in parallel while the 16 source fibers illuminated the surface successively. The measurements from the detection fibers that were close to the illuminating source

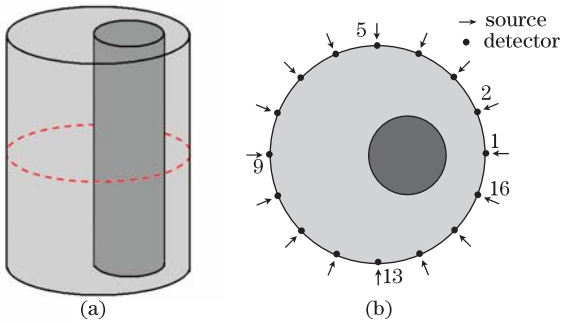

Fig. 1. Illustration of the phantom and the experimental setup with the sources and detectors located along the center of the cylinder.

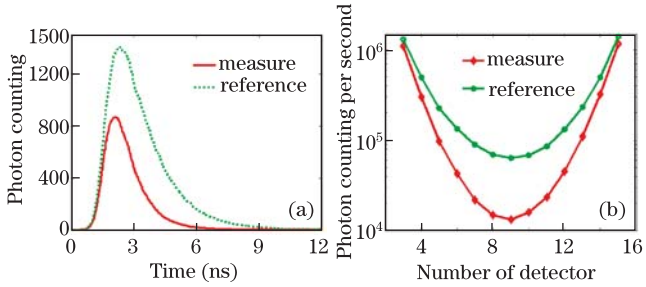

Fig. 2. (a) Measurements of the 5th detector for the 1st source from TCSPC system; (b) integrated intensity along detector channels for the 1st source.

fiber were abandoned, while the TPSFs from 13 detectors opposite to each source, i.e., the transmission mode, were employed for image reconstruction. This resulted in a total of 208 measurements. The TPSFs measured at the 5th detection site for both the homogeneous and heterogeneous phantoms in relation to the illumination of the first source are shown in Fig. 2(a). The dashed line denotes the measurement for homogenous phantom, while the solid line represents the measurement for the heterogeneous phantom. The results were normalized to the integration time of 1 s. By temporally integrating TPSFs for the homogeneous and heterogeneous phantoms, we acquired two sets of continuous-wave (CW) data, $\mathbf{y}_{\rm m} = [y_{\rm m}(\xi_1,\zeta_1), y_{\rm m}(\xi_2,\zeta_1),\cdots, y_{\rm m}(\xi_S,\zeta_D)]$ and $\mathbf{y}_{\rm r} = [y_{\rm r}(\xi_1,\zeta_1), y_{\rm r}(\xi_2,\zeta_1),\cdots, y_{\rm r}(\xi_S,\zeta_D)]$. These are illustrated in Fig. 2(b).

To eliminate the influence of the instrumental systematic and statistic noise on the reconstruction, as well as to suppress the amplitude scaling between the experimental and simulated data sets, a difference imaging scheme was employed in the experiment. In this scheme, the data sets measured for the heterogeneous phantom were calibrated by a reference measurement for the homogeneous one, i.e., a ratio $R(d,s) = y_{\rm m}(\xi_d,\zeta_s)/y_{\rm r}(\xi_d,\zeta_s)$ was calculated as the measurement data-type. Assuming that the instrumental responses are invariable, this difference scheme can cancel both the instrumental systematic error and the influence of the boundary coupling[10].

The 2D image reconstruction strategy is frequently used because of its computational economy framework. Many researchers have demonstrated that 2D reconstruction methods can recover optical properties in a cylindrical object where heterogeneous rods are embedded and aligned with a cylinder axis[11]. In this study, the ratio data-type of the two three-dimensional (3D) cylindrical phantoms was applied to the 2D shape-based tomographical reconstruction of a transverse plane of the heterogeneous phantom. To investigate the possibility and extent of reconstructing an image at a given plane from real (3D) experimental data with a 2D inverse model, the ratio data-type generated from the 2D and 3D forward models were compared. The numerical phantoms, with the same geometry as those of the experimental phantoms and background optical properties of $\mu_{\rm a} = 0.008$ mm^{-1} and $\mu'_{\rm s} = 0.8$ mm^{-1}, were employed for model comparison. The inclusion was set to a 3:2 target-to-background contrast in the optical properties. Figure 3(a) illustrates the ratio data-type calculated as a function of the source-detector separation for both homogeneous 2D and 3D cases. Figure 3(b) shows the ratio of the 2D data against the 3D data for the measurement type. The numerical result showed that the root mean square (RMS) for the 2D and 3D models was less than 6%, implying that the 2D reconstruction algorithm was adequate when using ratio data-type. To facilitate the evaluation of the reconstruction, an augmented cost function is defined as

$$E(k) = \sum_{s=1}^{S}\sum_{d=1}^{D}\left[R(d,s) - \frac{F_{d,s}(\mathbf{x}_k)}{F_{d,s}(\mathbf{x}_r)}\right]^2, \qquad (6)$$

where the denominator $F_{d,s}(\mathbf{x}_r)$ represents the 2D numerical model of the homogeneous phantom whose optical properties $\mathbf{x}_r$ were assumed as known and estimated by aforementioned homogeneous fitting algorithm.

We attempted to simultaneously reconstruct the optical properties of both the background and the inclusion, as well as the shape of the inclusion. The initial optical parameters chosen for the homogeneous background were $\mu_{\rm a} = 0.006$ mm^{-1} and $\mu'_{\rm s} = 1.1$ mm^{-1}; for interior region Ω_2, they were $\mu_{\rm a} = 0.01$ mm^{-1} and $\mu'_{\rm s} = 1.0$ mm^{-1}. The boundary Γ_2 of the inclusion was described by 5 Fourier coefficients for each Cartesian coordinate, x and y. A regular mesh with 64 vertex nodes and 64 edges was discretized for the BEM calculation. A circular curve with a diameter of 8 mm centered at $0,0$) was selected as the initial guess for the shape reconstruction. The expected values, initial estimates, and reconstructed values of the optical parameters are listed in Table 1. Results show that although the wave numbers k_ℓ are recovered with quite good accuracy, the

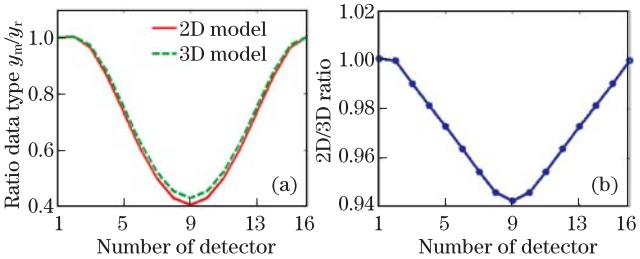

Fig. 3. (a) Comparison of ratio-type data generated from 2D (solid curve) and 3D (dashed curve) forward models; (b) ratio of 2D/3D data versus the sequence number of detectors.

Table 1. Reconstructed Values of the Optical Coefficients for the Test Phantom

Region	Optical Parameter	Expected Value (mm^{-1})	Initial Guess (mm^{-1})	Reconstructed Value (mm^{-1})
Background	$(\mu_{\rm a1}, \mu'_{\rm s1})$	(0.0044, 1.69)	(0.0060, 1.10)	(0.0053, 1.43)
	$k_1 = \sqrt{3\mu_{\rm a1}\mu'_{\rm s1}}$	0.149	0.141	0.151
Inclusion	$(\mu_{\rm a2}, \mu'_{\rm s2})$	(0.0150, 1.50)	(0.0100, 1.00)	(0.0155, 1.42)
	$k_2 = \sqrt{3\mu_{\rm a2}\mu'_{\rm s2}}$	0.260	0.173	0.257

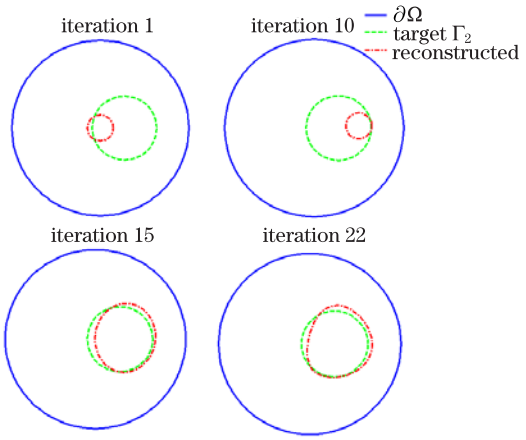

Fig. 4. 2D recovery of the inhomogeneity shape from 3D experimental measurements.

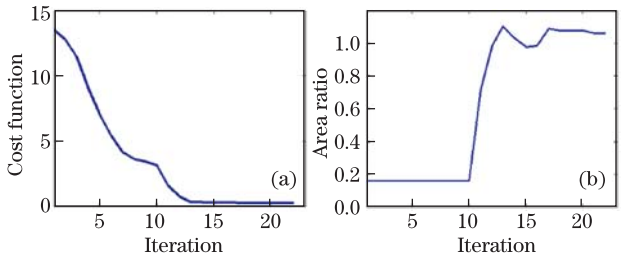

Fig. 5. Evolution of different measures versus iteration index: (a) the cost function; (b) the ratios between reconstructed and target areas.

absorption and scattering coefficients of both the background and inclusion can be reconstructed with some deviations from the expected. This observation was consistent with the conclusions derived by Arridge *et al.* wherein simultaneous unique recovery of the absorption and diffusion coefficients might not be achieved with a CW data-type[12].

To stabilize the algorithm, the center of the inclusion and the optical properties of the background in the initial iterations were reconstructed based on the initial guess of the shape and the optical properties of the inclusion. The complete set of the unknowns were incorporated into the reconstruction for further iteration. The process of shape reconstruction is demonstrated in Fig. 4, where the dashed circles represent expected shape and the dotted dashed ones are the reconstructed shape. The location and boundary of the inhomogeneous region were recovered with accepted accuracy in the last iterations.

To quantify the efficacy of the proposed method, the cost function versus the iteration index was calculated, as shown in Fig. 5(a). Since the measurements were especially sensitive to the optical parameters of the background, the cost function decreased rapidly during the first 6 iterations. The cost reached a local minimum in the successive iterations due to the successful recovery of fine details for both the shape and the optical properties. To reinforce the evaluation, the recovered area of the inclusion was employed as the second measure, which was calculated by the curvilinear integral formulation. The expected area of the inclusion was 314 mm^2 while the area of the starting shape was 50 mm^2. Figure 5(b) shows the ratio of the reconstructed area to the target area as a function of the iteration number. The reconstructed shape finally reached an area of 333 mm^2, indicating good approximation of the target area.

In conclusion, we present a 2D shape-based reconstruction scheme for steady-state DOT, which can simultaneously recover boundary-describing parameters of the regions and their respective interior constant optical properties. The experiment demonstrates the effectiveness of the proposed methodology. Results show that although the shapes of the interior domains can be well recovered, the simultaneous accurate reconstruction of the absorption and scattering coefficients is difficult to achieve by using only CW measurement. However, with CW measurements, the reconstruction of the wave number of the Helmholtz equations is quite precise.

This work was supported by the National Natural Science Foundation of China (Nos. 30870657 and 30970775), the National Basic Research Program of China (No. 2006CB705700), the National High Technology Research and Development Program of China (No. 2009AA02Z413), and the Tianjin Municipal Government of China (Nos. 09JCZDJC18200 and 10JCZDJC17300).

References

1. F. Gao, L. Zhang, J. Li, and H. Zhao, Chin. Opt. Lett. **6,** 889 (2008).
2. Y. Tan and H. Jiang, Appl. Opt. **47,** 2011 (2008).
3. F. Yang, P. Ruan, F. Gao, and H. Zhao, Chinese J. Lasers (in Chinese) **36,** 2517 (2009).
4. A. D. Zacharopoulos, S. R. Arridge, O. Dorn, V. Kolehmainen, and J. Sikora, Inverse Problem **22,** 1509 (2006).
5. P. Ruan, Y. Liu, F. Gao, H. Zhao, and F. Yang, Acta Opt. Sin. (in Chinese) **29,** 2421 (2009).
6. V. Kolehmainen, S. R. Arridge, M. Vauhkonen, and J. P. Kaipio, Phys. Med. Biol. **45,** 3267 (2000).
7. J. Sikora, A. Zacharopoulos, A. Douiri, M. Schweiger, L. Horesh, S. R. Arridge, and J. Ripoll, Phys. Med. Biol. **51,** 497 (2006).
8. R. Cubeddu, A. Pifferi, P. Taroni, A. Torricelli, and G. Valentini, Phys. Med. Biol. **42,** 1971 (1997).
9. S. J. Madsen, M. S. Patterson, and B. C. Wilson, Phys. Med. Biol. **37,** 985 (1992).
10. H. Zhao, F. Gao, Y. Tanikawa, K. Homma, and Y. Yamada, Appl. Opt. **44,** 1905 (2005).
11. M. Schweiger and S. R. Arridge, Appl. Opt. **37,** 7419 (1998).
12. S. R. Arridge and W. R. B. Lionheart, Opt. Lett. **23,** 882 (1998).